JOURNAL OF BIOLOGICAL REGULATORS & HOMEOSTATIC AGENTS Vol. 33, no. 6, 1725-1736 (2019)

POTENTIAL ROLE OF MAGNETIC RESONANCE BRAIN RELAXOMETRY IN VETERINARY MEDICINE: A PRELIMINARY STUDY

F. DEL SIGNORE, M. VIGNOLI, G. MARRUCHELLA, F. SIMEONI,
R. TAMBURRO, G. ASTE and F. DE PASQUALE

University of Teramo, Piano D'Accio, Teramo, Italy

Received May 25, 2019 - Accepted September 9, 2019

Magnetic Resonance (MR) is a non-invasive modality of choice for the evaluation of brain morphology, with superior performance as compared to other techniques. However, MR images are typically assessed qualitatively, thus relying on the experience of the involved radiologist. This may lead to errors of interpretation in the presence of subtle alterations and does not exploit the full potential of this technique as a quantitative diagnostic tool. To this end Magnetic Resonance Relaxometry (MRR), which is able to quantitively characterize the tissues under investigation through their relaxation rates, seems extremely promising. Many studies assessed the feasibility of relaxometry as a diagnostic tool in human brain disorders, with the most promising results obtained in the evaluation of neurodegenerative diseases and in the oncologic field. However, despite such extensive literature in human medicine, due to the lack of standardized protocols and the need of high-field MRI scanners, to date few studies have been performed on companion animals. In this work, first we describe relaxometry applications in human neuropathology and their possible extension to companion animals both in the experimental and clinical fields. Then, we present two experiments performed on a typical standard clinical scanner operating at 0.25 T to show that, despite the low field intensity, this technique may be promising even in the clinical setup. We tested the relaxometry protocol in a phantom study and then applied it to a real clinical case study. The results showed that this protocol used on a phantom led to a higher contrast, as compared to the standard approach. Furthermore, when applied to a real case study, this protocol revealed brain lesions undetected by the standard technique which were confirmed by a histopathological examination. These preliminary results are encouraging and support the development of this approach as an advanced diagnostic tool even in a clinical setting where low field MRI scanners are typically employed.

Relaxometry refers to a Magnetic Resonance Imaging (MRI) quantitative technique developed to estimate the relaxation times of the tissues under investigation. This approach is an emerging and promising technique which aims at exploiting the full potentiality of MRI as a quantitative diagnostic tool (1). In fact, although MR is the modality of choice for the evaluation of brain morphology, as compared to CT (2), images are typically assessed qualitatively, thus relying on the experience of involved radiologists. This has severe drawbacks (e.g. errors of interpretation in presence of subtle alterations and unfeasibility of multi-center studies) which are overcome with MR Relaxometry (MRR) where individual contrast mechanisms (e.g. T1, T2 and T2*) of the tissues under investigation are

Key words: brain; magnetic resonance; relaxometry; dog; cat

Corresponding Author:
Francesca Del Signore DVM,
University of Teramo,
Piano D'Accio,
64100, Teramo, Italy
Tel.: +39 3409736807
e-mail: fdelsignore@unite.it

0393-974X (2019)

isolated and quantified (1, 3). Such mechanisms and the basic MRR concepts are summarized in the next section.

Several applications of MR relaxometry to human medicine have been reported, e.g. in the oncologic field, epilepsy and neurodegenerative disorders (4-10), however, in veterinary medicine, few studies have been performed on brain disorders affecting canine and feline patients. For feline species, the first study was performed by Kamman et al. to assess whether T1 and T2 relaxation times could characterize brain edema experimentally induced in feline brains (11). They showed that there was a linear correlation between water content and T1 and T2 relaxation times. The second study, performed on cats at 4.7 T, investigated T2 abnormalities in case of experimentally inoculated glioma (12). It was shown that at the time of maximal tumor growth and edema spread, a tissue differentiation was possible through MRR parameter maps (12). Regarding canine species, in addition to experimental studies (13), in a recent study (14) the authors tried to quantitatively detect hippocampal abnormalities in epilepsy to be used in the veterinary practice. The results suggest that individual analysis might be a suitable method to prove hippocampal involvement in epileptic dogs (14).

After what has been illustrated regarding MRR applications in human medicine, the fundamental question is ‘can we perform MRR by adopting standard clinical scanners to obtain new clinical insights in veterinary medicine?’ We believe that this is the real challenge for MRR to become an advanced diagnostic tool.

In this work, firstly we introduced the above MRR parameters, e.g. T1 and T2. Secondly, we discussed the current literature on this topic in canine and feline species and the possible applications based on human medicine, where this technique has been largely tested. Thirdly, we report an original phantom-based study to explore the feasibility of this approach using the typical experimental setup available in the clinical field. The aim is to assess whether MRR can be useful to differentiate tissues which cannot be detected by the standard clinical scans. This allowed us to test the potentiality of the MRR protocol which was then applied to a second experiment where we studied the brain of an euthanized dog in order to test whether it was possible to identify lesions which had been undetected by the standard T1/T2 weighted images. Finally, these findings were validated by a histopathology study. Notably, our preliminary tests were performed with a low field scanner (operating at 0.25 T) since this is typically employed in the vast majority of veterinary facilities (15).

MATERIALS AND METHODS

MRR relaxation times T1 and T2

In conventional MRI, the tissue contrast is obtained by adjusting the sensitivity of the acquired signal to differences in the tissue T1, T2 and T2* characteristic relaxation times (T1, T2 and T2*-weighted images) (1). Since T1, T2 and T2* are influenced by local biophysical structure and biochemical environment, alterations in T1 and T2 can be associated with disease (e.g. edema, tumor invasion and axonal de-myelination) or other biological processes such as neuro/development-degeneration-plasticity, learning and aging (3, 16). Therefore, to obtain information on tissue structure and function in a quantitative manner (and theoretically independent of scanner hardware and sequence parameters) MRR extracts the relaxation times from the MRI data (1). This is achieved through the adoption of a model describing the MRI signal evolution as a function of the relaxation parameters and a fitting procedure to estimate from the acquired signals, T1, T2 and T2* (1). Many T1/T2w images have to be repeatedly acquired to sample the recovery/decay of the MR signals corresponding to the acquisition through either Inversion Recovery (IR)- or Spin Echo (SE)-based sequences (1). For the T1 estimation, although both IR and SE can be adopted, in this study, an SE sequence was adopted for two reasons. Firstly, the SE acquisitions are faster than IR and this is a fundamental aspect in veterinary medicine since the patients are anesthetized and a long general anesthesia is dangerous. Secondly, SE sequences can be adopted by varying a single parameter (Repetition Time TR) that is accessible to the user in all standard scanners/software. On the contrary, to adopt IR sequences for relaxometry, the standard scanner software needs to be modified in order to give access to other parameters such as the Inversion Time (TI) to the user. Once the final T1/T2 map is obtained this can be overlaid to the anatomical

MRI data to spatially localize the eventual brain lesions.

The typical acquisition and analysis pipeline are shown in Fig. 1. Despite this technique being promising, it is not without disadvantages. For example, common sources of error are due to residual or incoherent transverse magnetization and movement artifacts (3). In fact, beyond bulk motion, physiological motion, including blood flow, can also induce subtle artifacts and bias in T1 and T2 values (3). Furthermore, accelerated measurement techniques, usually adopted to speed up the acquisition time, generally use small flip angle radiofrequency pulses to sample the magnetization which are characterized by a low signal to noise ratio (SNR). To increase the SNR, as an example, systems based on multichannel detection can be used.

Moreover, the subject motion due to the longer scanning time of MRR as compared to standard MRI, lead to important artifacts affecting the final T1/T2 maps. This can be particularly problematic in multi-slice acquisitions, where the slice selection may result inaccurate due to differences of times, echo times or flip angles (1). Notably, this aspect can be minimized in veterinary medicine thanks to the general anesthesia.

Experiment 1 – Phantom study

The basic idea behind this experiment was to compare the minimum contrast detectable through a T1-based approach with what can be evidenced with an MRR technique. Data was acquired from two phantoms (P1 and P2) composed of NaCl 0.9% solution (B. Brown, Melsungen, Germany) doped with different concentrations of a contrast agent (CA), namely Magnegita (Gadopentetate dimeglumine 500µmol/ml, Agfa HealthCare Imaging Agents GmbH, Köln, Germany). P1, filled with 5 µmol of CA, represented the reference, and thus remained constant throughout the experiment. In P2, instead, the concentration of the CA was gradually varied in order to consider three separate conditions. The MR data were acquired by means of an Esaote Vetscan Grande scanner operating at 0.25 T equipped with a NeuroCoil 2 (Esaote S.PA, Genova, Italy). In each condition, two sets of MRI data were acquired. The “clinical” dataset (CLI), i.e. obtained with clinical sequences, was acquired by an SE T1w sequence with standard typical settings on a dorsal plane (TR = 200 ms, TE = 26 ms, FOV = 210x210 mm^2, slice thickness = 2 mm, Gap =0 mm, Matrix 384x368, Number of acquisition-NEX =2). The second dataset, related to the relaxometry and denoted by ‘REL’, was acquired with an ad-hoc developed protocol consisting of repeated acquisitions of SE T1w images corresponding to a variable TR in the range [150, 900] ms with the same other parameters setting. The first interval [150 800] ms was sampled every 50 ms, while the interval [800 900] ms was sampled every 100 ms. This selective sampling represented a compromise to allow a denser sampling in the most rapid part of the relaxation curve while saving some acquisition time. For the data analyses, these consisted of fitting the acquired signals with a two-parameter model by means of an unconstrained minimization based on derivative-free method (17). These analyses were performed by means of in-house developed codes in MATLAB (MATLAB and Statistics Toolbox Release 2015b, The MathWorks, Inc., Natick, Massachusetts, USA).

Experiment 2 – Single case study

In this case, the protocol developed in Experiment 1 was applied to a real clinical case. A 9 year-old male German shepherd was referred to our hospital because of anorexia and vomiting; atopic dermatitis treated with cyclosporine and *Escherichia coli* (*E. coli*) multiresistent cystitis were recorded in the patient history. Left head tilt and bilateral nystagmus were observed during physical examination. Soon after the referral, rapid worsening of clinical conditions occurred, and euthanasia was elected by the owner; a post mortem MRI of the brain was performed. All the procedures were performed with the owner’s compliance. Sequences T1w, T2w and FLAIR were acquired in different planes with the same scanner and coil used in Experiment 1. Sequences SE T1w, FSE REL T2w and FAST FLAIR were acquired with the settings as follows. For SE T1w transverse scan: TR= 1350 ms, TE= 26 ms, Matrix 320 x 288 and FOV 240 x 240 mm^2, for SE T1w sagittal plane: TR=1500 ms, TE=26, Matrix 384x 240 and FOV 180x180 mm^2, for the FSE REL T2w sagittal sequence: TR= 7780, TE= 90 ms, FOV 250x250 mm^2, Matrix 400x352, for FSE REL T2W: TR= 8640, TE= 90, Matrix 488x352 and FOV 260x260 mm^2, for FLAIR dorsal scan: TR=6670, TE=90 ms, FOV 230x230 mm^2, Matrix 288x224 and Number of Acquisition- NEX =1. Slice thickness = 3 mm and Gap=0.4 mm were set for all the sequences and Number of Acquisition - NEX

=2 for all T1w and T2w sequences. The MRR protocol was then applied to the central 2 mm sagittal slice in order to obtain a representative sampling of the brain while limiting the long acquisition time as compared to 3D multi-slice approach. During the acquisition, a set of SE T1w images corresponding to a variable TR in the range [50, 1100] ms were acquired. The first interval [50 300] ms was sampled every 150 ms, while the interval [350 1100] ms was sampled every 50 ms. Data analysis was performed with the same analysis steps described for Experiment 1. In order to validate the MRR results and thus to assess the nature of these lesions, necropsy and the histopathological analysis were performed. The entire brain was collected, fixed in 10% neutral buffered formalin, embedded in paraffin and routinely processed for histopathological investigations. In particular, 4-µm thick sections were stained with hematoxylin and eosin and observed under a light microscope (model ECLIPSE E600W, Nikon, Japan).

RESULTS

Experiment 1

In this experiment, three separate scenarios were considered. Firstly, we studied a control condition where P1 and P2 have a significant different concentration of CA, 5 *vs* 3 µmol, respectively. In this case, as can be seen in Fig. 2, where T1w images are reported, the contrast in the ‘CLI’ data is sufficient to clearly distinguish P1 (Fig. 2A) from P2 (Fig. 2B). A visual inspection by an expert radiologist can easily identify such difference. The idea was then to decrease the difference in the concentration between P1 and P2 to check whether there is a condition where this difference is so small that in the ‘CLI’ data P1 and P2 cannot be distinguished while in the ‘REL’ data these result separated. We started from a control condition where the P1 and P2 CA concentrations were identical (Fig. 2 C-D). In this case, no evident contrast can be observed between P1 and P2 from ‘CLI’ data. On ‘REL’ data the estimation of T1 was run. As an example, Fig. 3 demonstrates the comparison between the evolution of the acquired and the predicted signal (dashed line) based on the estimated parameters. A good agreement between the acquired and predicted signal can be noted, thus suggesting a successful fitting procedure. The obtained T1 maps are shown in Fig. 2 E-F and, as expected, also in this case the visual inspection did not reveal significant differences in the two phantoms. To quantify these observations, in Table I mean values (µ) and standard errors (Standard Error of the Mean- SEM) are compared of the ‘CLI’ signals and T1 values. To quantify the contrast, the absolute value of the percentage variation between the two phantoms defined as $\Delta = (\mu_1 - \mu_2)/\mu_1$ are shown (Table I). In this case, the same percentage variation was observed between P1 and P2 both from ‘CLI’ and ‘REL’ data. This confirms that no artefactual higher contrast, as expected, is obtained from T1 maps.

Table I. *Phantom study - same contrast agent concentration.*

	Clinical Signal Values (au) µ±SEM (ms)	T1 Map values µ±SEM (ms)
P1	1074±1	56.3±0.8
P2	1110±1	58.0±0.8
Δ%	3%	3%

mparison between clinical and T1 values from phantoms with the same contrast medium centration. As expected, no significant differences are obtained in both CLI and REL data.

Table II. *Phantom study - different contrast agent concentration (0.5 µmol).*

	Clinical Signal Values µ± SEM (au)	T1 Map Values µ± SEM (ms)
P1	1082±1	57.2±0.7
P2	1092±2	49±1
Δ%	1%	12% **

*Comparison between clinical and T1 values from phantoms corresponding to different CA concentrations (P1: 5 µmol and P2: 5.5 µmol). A significant increase in the contrast is obtained in REL as compared to CLI data. The percentage variation (Δ) is twelve times higher and a t-test reveals a statistically significant difference in REL data (** $p < 0.01$).*

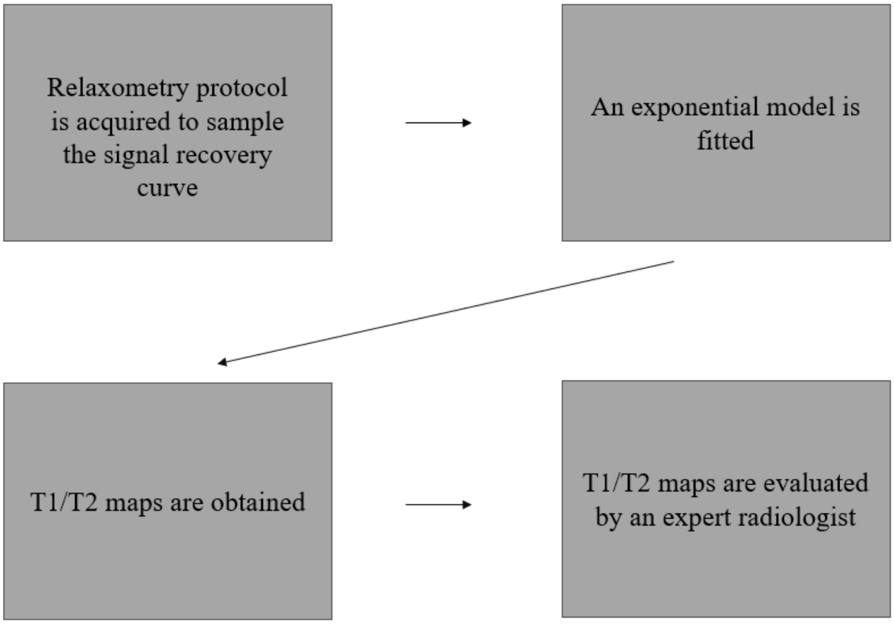

Fig. 1. *Summary scheme illustrating the pipeline to perform MRR studies.*

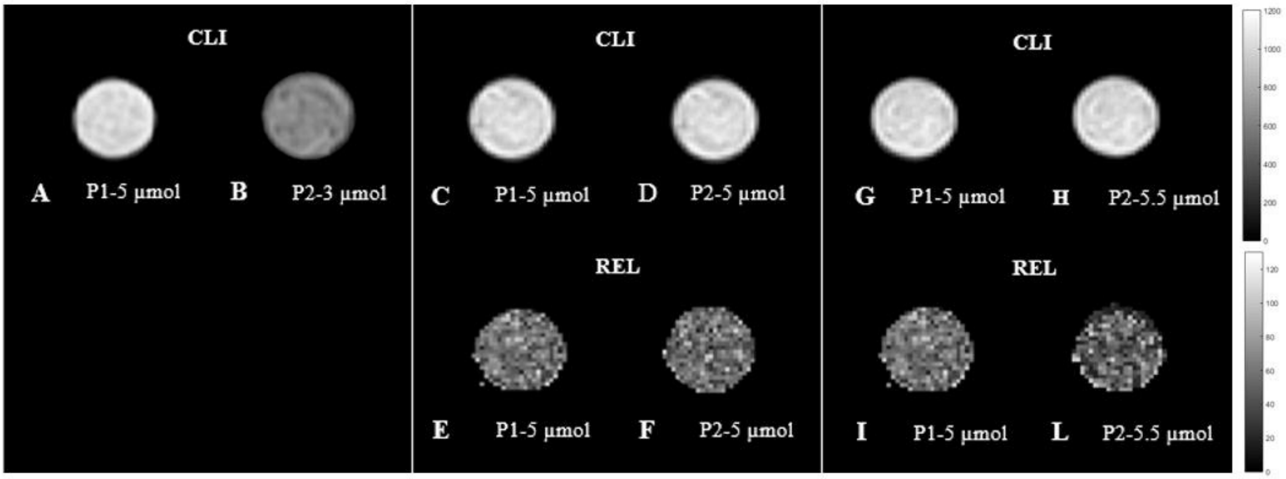

Fig. 2. *Comparison between the Clinical (CLI) and Relaxometry (REL) results. On the right, color bars indicating the signal intensity expressed in au for CLI and in ms for T1 maps.* ***A, B****) Comparison between CLI data acquired with a SE-T1w dorsal scan on phantom P1 doped with 5 µmol of CA (A) and on phantom P2 doped with 3 µmol of CA (B); it can be noted the high contrast in signal difference between P1 and P2 clearly identifiable by visual inspection.* ***C-F****) CLI data acquired with a SE-T1w dorsal scan on phantom P1 and P2 doped with 5 µmol of CA (C, D) and REL data showing T1 maps obtained from P1 and P2 (E, F); in both T1w and T1 maps no visual difference can be detected; this is an important check on the false positives.* ***G-L****) CLI data acquired with T1w dorsal images of P1 filled with 5 µmol of CA (G), CLI data of P2 filled with 5.5 µmol of CA (H) and respective T1 maps (I-L); while from T1w images no difference can be detected, the T1 map of P2 is clearly darker than P1. This difference is statistically significant ($p<0.01$) and consistent with the underlying physics, i.e. increasing CA concentration we expect T1 to progressively decrease.*

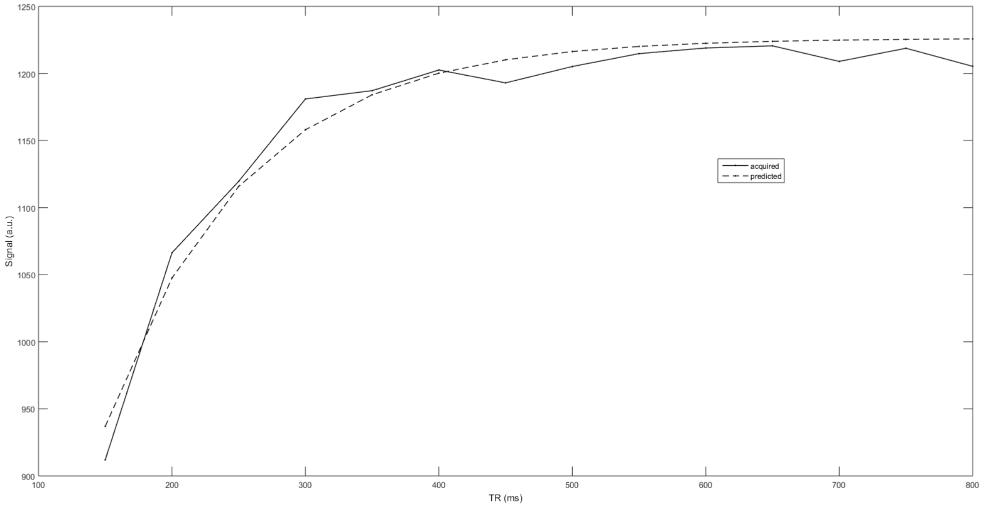

Fig. 3. *As a representative example, the results of the fitting procedure for a voxel are shown. Good agreement can be noted between the acquired (solid line) and predicted (dashed line) signal by the model based on the estimated T1 and proton density.*

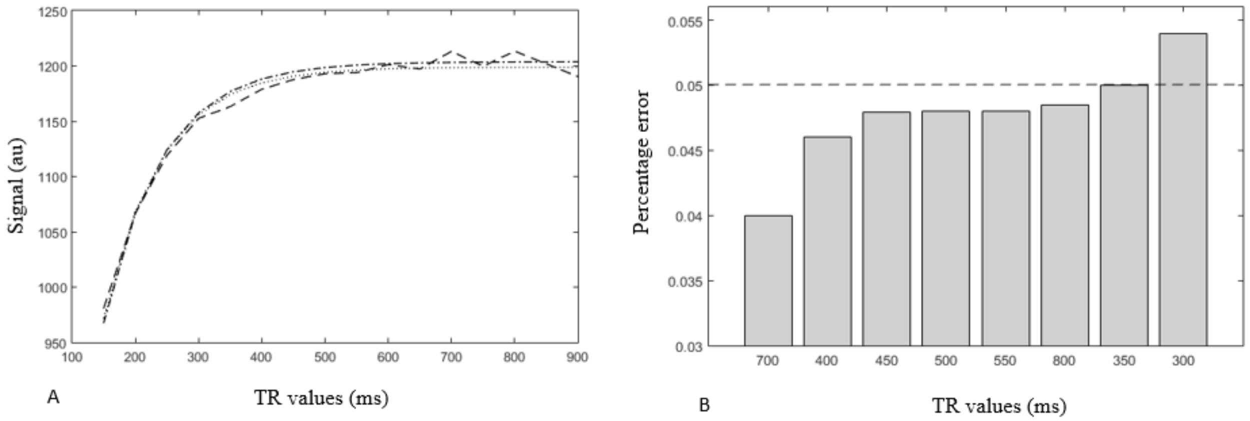

Fig. 4. ***A****) As an example, the MR signal predicted by the two-parameter model using the original 15 TR values from the 'true' T1 estimate (dashed-dotted line). The dotted line rshows the signal obtained from the same model with the T1 estimated. The dotted line shows the signal computed from the T1 estimate obtained using only 8 TR values.*

B*) The incremental percentage error is reported as a function of the TR values iteratively removed from the model. It can be noted that the adopted threshold (5%) is exceeded at TR = 300 ms.*

In the next scenario (Fig. 2 G-L), the CA concentration was increased in P2 to 5.5 µmol (P1 CA concentration fixed to 5 µmol). As seen in Fig. 2 G-H, no contrast is apparent from a visual inspection from 'CLI' data. This is confirmed by the values reported in Table II where the average values in P1 and P2 are not statistically different, as revealed by a *t*-test, and the percentage change is around 1%. This supports the evidence of a negligible contrast in 'CLI' data between P1 and P2. On the other hand, as shown in Fig. 2 I-L (REL data), some contrast is evident between P1 and P2 from the visual inspection. It can be noted that T1 values in P2 are smaller. This is correct, since the higher the CA concentration, the lower T1 values (as expected by the physic properties of the CA itself in shortening T1 relaxation time (18). This is confirmed by the values reported in Table II. The mean values are significantly different (** $p<0.01$) and the percentage change is twelve times larger than in the 'CLI' data. Therefore, in this case, the contrast obtained in the T1 map is one order of magnitude higher than with the standard MRI procedure. These results are promising in showing that a higher contrast can be achieved with MRR, revealing potential subtle differences among tissues that the standard approach could not detect.

However, an important limitation, especially in the clinical field, relates to the large acquisition time required by the MRR protocol. As matter of fact, in the above analysis, a set of 15 TR values was used in order to estimate a reliable T1 map. This leads to a total acquisition time of 90 minutes that might result prohibitive in clinical settings. Therefore, we tried to quantify the stability of the T1 estimate corresponding to a smaller and 'optimal' subset of the TR values. The general idea is to compute the distance between the T1 values obtained from all TRs and from a subset of them. Then, such distance was minimized as a function of the set of TR explored. Initially, the T1 mean and standard deviation reported Table I for phantom P1 was considered as a reference. By means of a Gaussian distribution based on these values, 200 T1 values were sampled. Then, by inputting such values in the two-parameter model adopted in this study (see above), 200 MR signals were simulated. Finally, some noise estimated in the background of the 'real' acquired data was added. The standard deviation of the acquired signals was estimated and then noise sampled from a Gaussian distribution was added

Table III. *MRI* vs *advanced MRI.*

	MRI	ADVANCED MRI
ADVANTAGES	Non-invasive No X-Rays Greater contrast in soft tissues respect on CT Multiple sequences-different contrasts	Non-invasive Quantitative and objective Evidence of undetectable lesions with qualitative scans No extra costs in term of diagnostic tools Signal analysis performed off-line
DISADVANTAGES	Longer scan protocol respect on CT General anesthesia necessary for pets	Longer scan protocols respect on MRI Extra skills for radiologists to analyze maps Errors in relaxation times estimation

Summary of advantages and disadvantages of the application of relaxometry compared to clinical studies.

with mean zero and such standard deviation. In Fig. 4A (broken line) an example a simulated signal is shown. Then the fitting procedure was run. Initially, all the TR values were used and the corresponding T1 estimates were adopted as reference ('true') values. In Fig. 4A, is an example of a signal simulated form a 'true' T1 value (dashed-dotted line). Then, one TR value was removed and the 200 T1 estimates were repeated. This was carried out for all the possible TR values and every time the percentage error between the 'true' and the estimated T1 values was computed. Afterwards, the TR leading to the smallest error was selected. If such value was smaller than 5%, that value was removed from the subset of TR considered. This procedure was repeated for the next TR value to be removed and it stopped when the cumulative percentage error reached 5%. Seven TR values obtained, namely [700 400 450 500 550 800 350] could be removed, see Fig. 4B where the cumulative error is reported. As an example, in Fig. 4A (dotted line) the signal simulated from the model when these 7 TR values were removed (in Fig. 4B the T1 estimate obtained from the 'reduced' model was used in the complete model, i.e. using all the TR values, for display reasons).

These results are encouraging, showing that with the smaller number of TR values obtained the quality of the estimate is still acceptable. Notably the acquisition time reduces from 90 to 40 minutes.

Experiment 2

In the real case study, in T2w and T1w images, slightly hyperintense lesions were detected at the level of pons and medulla oblongata in every scan (Fig. 5, solid white arrows) and in both T1w and T2w scans the fourth ventricle was barely visualized

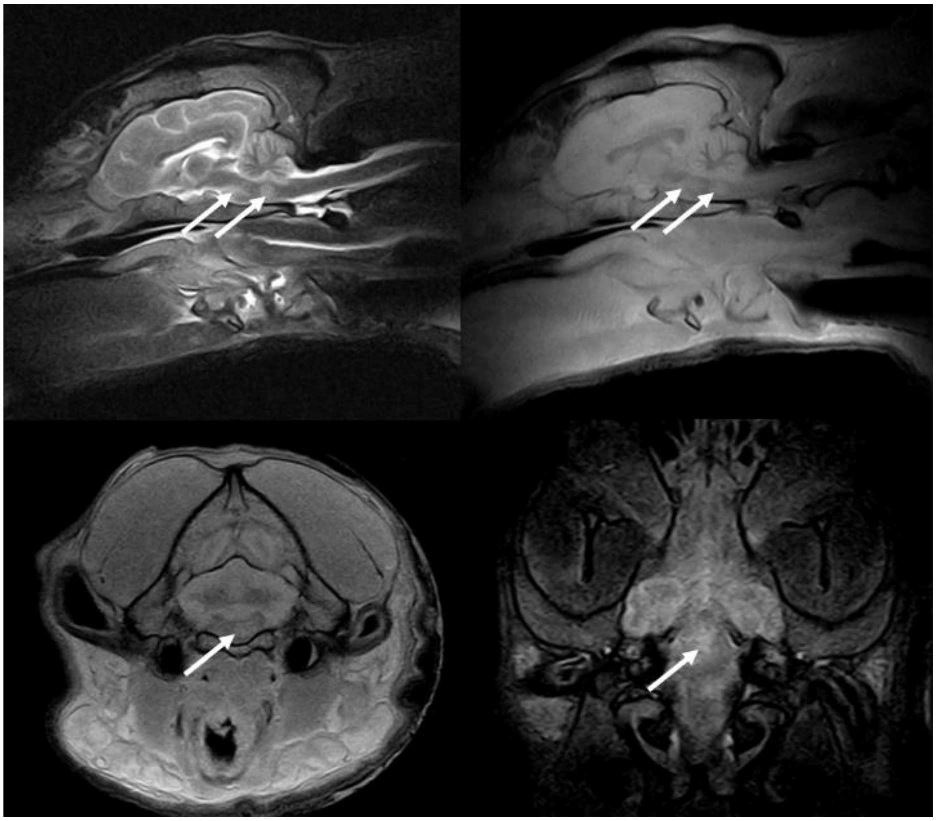

Fig. 5. *A) FSE REL T2w sagittal scan;* ***B)*** *SE T1w sagittal scan;* ***C)*** *SE T1w transverse scan;* ***D)*** *dorsal FAST FLAIR scan. White solid arrows point at hyperintense lesions at the level of pons and medulla oblongata evident in every scan acquired. The fourth ventricle is not evident.*

(Fig. 5 A-B). These lesions were suspected to be inflammatory or vascular. In the sagittal and transverse T2w image of the cerebellum (Fig. 6 A-B), a slight hyperintense lesion was detected. Notably, this lesion was not evident in T1w images (Fig. 6C, solid white arrows). Furthermore, it can be noted that, at the level of the pons and the medulla oblongata, hyperintense areas are present both in T1w and T2w images (Fig. 6 D-F, solid white arrows). Of note, in the T1 map, some additional hyperintense regions were observed in the area usually occupied by the fourth ventricle and at the level of the cerebellar parenchyma (Fig. 6 D-F, solid black arrows). These observations are in line with the histopathological study. The brain sections to be sampled were identified by comparing the sagittal images with the transversal ones (Fig. 6G - white line). Within the sampled area (reported in Fig. 6H – white square), grossly and scattered hemorrhages were identified at the level of the pons, medulla oblongata, cerebellar vermis and parenchyma (Fig. 6I, white solid and dashed arrows). Histologically, foci of acute vasculitis and fibrinoid necrosis were observed at the same level (Fig. 7A, solid white arrow). Necrotic-hemorrhagic areas, mainly infiltrated by polymorphonuclear cells, were also observed in the surrounding parenchyma and, notably, a large hemorrhagic area was evident within the white matter of the cerebellum (Fig. 7B,

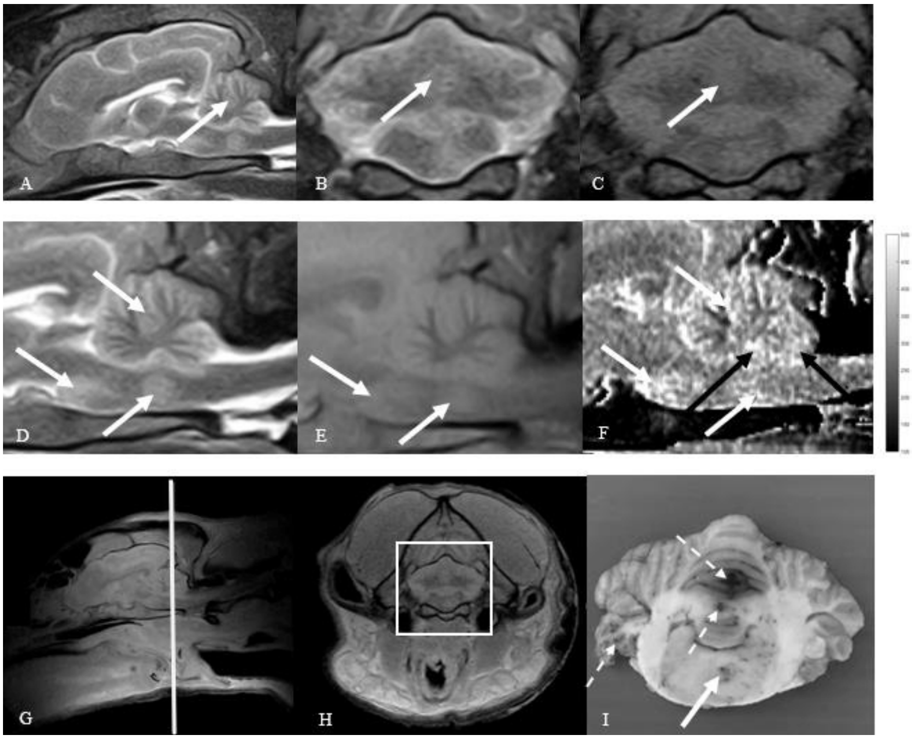

Fig. 6. ***A)*** *FSE REL T2w sagittal scan;* ***B)*** *FSE REL T2w transverse scan;* ***C)*** *SE T1w transverse scan. White solid arrows point at the cerebellar hyperintense lesion detected in T2w images; notably, at the same level, no abnormalities are visible in T1w image.* ***D-F)*** *Comparison between the T2w sagittal image (D), the T1w sagittal image (E) and T1 map of pons, medulla oblongata and cerebellum (F); white solid arrows point at hyperintense lesions at the level of pons, medulla oblongata and cerebellar evidenced by both T1 map and clinical scans. In the T1 map, black solid arrows point at hyperintense areas at the level of cerebellar parenchyma and at the level of the area surrounding the fourth ventricle not detected by clinical scans. On the right of T1 map, the color bar of the signal is demonstrated. G-I) correspondence between MRI data and corresponding anatomical sections used for the histopathological study; in T1w sagittal section (G), the white line represents the transverse section of vermis cerebelli and medulla oblongata that has been sampled for histological examination, evidenced by the white square (H); in the transverse anatomical section (I) scattered hemorrhages can be observed at the level of cerebellar parenchyma (dashed white arrows) and of the medulla oblongata (solid white arrow).*

solid white arrow). Therefore, histopathological examination confirmed the presence of cerebellar lesions barely detected by clinical T1w scans, and the nature of the lesion was consistent with what was suspected after MRI examination.

The detection of brain lesions related to vasculitis is of interest. While in human medicine this condition is currently detected with high field scanners (19), little information is available on the pathologic mechanisms that result in this disorder in dogs (20); in veterinary medicine few reports are available on this condition, none of which describe MRI findings (20-23).

DISCUSSION

Nowadays, in veterinary medicine, few relaxometry studies have been to investigate canine and feline brain disorders and the application of this technique in the clinical practice. In this study, we report preliminary results obtained both on phantoms and real data experiments performed with a low field scanner. We obtained that, in phantoms, MRR can reach a higher contrast than in clinical scans. Notably, when applied to a real clinical case, as compared to the clinical protocol, MRR was able to characterize better cerebellar abnormalities that were confirmed by histopathological examinations. These results are encouraging, although this work was performed only post-mortem, and the contribution of post-mortem abnormalities in MRR must be thoroughly investigated in successive studies.

In general, to develop advanced techniques, such as MRR, in veterinary medicine it may be useful to improve diagnosis/treatments of brain diseases, as in human medicine, especially in cases of disorders causing only subtle changes (e.g., hepatic encephalopathy or distemper encephalitis) that can be easily missed without an adequate resolution scanning and careful interpretation (24). However, this technique presents some disadvantages that makes its widespread application difficult, such as a long acquisition time in patients under general anesthesia (see Table III for a summary of the main drawbacks of this approach). In this work, to show the potentiality of this approach in the typical clinical setup, we used the standard equipment typically provided in the clinical field. To reduce the large acquisition time, we adopted SE sequences (faster than typically employed IR) and we optimized

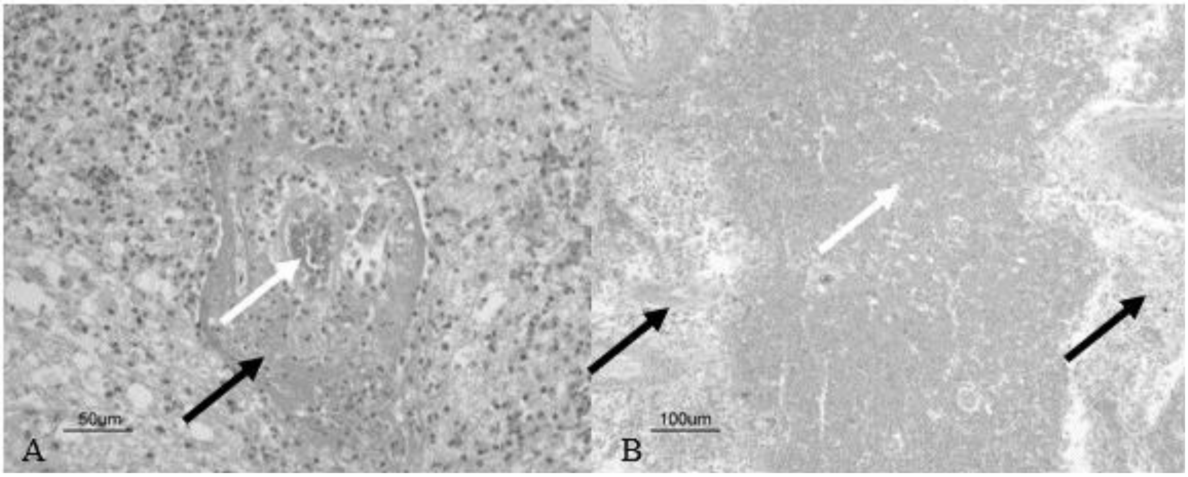

Fig. 7. *Histological examination of medulla oblongata and vermis cerebelli.* ***A****) Medulla oblongata: a blood vessel (solid white arrow) is surrounded by the deposition of hyaline, "fibrinoid" material (solid black arrow). The presence of a mixed inflammatory infiltrate is also evident. Haematoxylin and eosin stain. Final magnification: x 200.* ***B****) vermis cerebelli: a large haemorrhagic area (solid white arrow) is present within the white matter of the cerebellum (solid black arrow). Hematoxylin and eosin stain. Final magnification: x 100.*

the number of TR employed through a simulation study. Furthermore, while anatomic sections for histopathological analysis are usually performed in the transversal plane, we computed the T1 map in a sagittal slice to acquire as much cerebral parenchyma as possible with a single acquisition protocol, limiting as much as possible post mortem deterioration artifacts.

It must be stressed that typically in human medicine as well as in animal model studies (25) MRR is typically performed with high field scanners (≥1.5 T), while in veterinary facilities the magnetic fields employed are in the order of a few hundred mTs (15). This limits the spatial resolution and in general the possible applications of this technique. To overcome this limitation, a possible approach could be the use of cross-modality co-registration approaches suitable to co-register single or a few slices from an image obtained by a modality (e.g. the histopathological image) to a volume obtained by another modality with different spatial resolution (e.g. the T1-maps) (26,27).

In conclusion, MRR is a useful technique currently applied to human brain disorders, however, in veterinary medicine the literature is limited but increasing, with recent MRR studies performed on neurological (14) and orthopedic fields (28). In line with these works, the results reported here suggest that this technique may be promising and pave the way for further studies on MRR as an advanced diagnostic tool to be associated with routine clinical scans. In future studies, this technique might be applied in case of inflammatory/infectious or metabolic disorders (e.g distemper encephalitis, hepatic encephalopathy) to detect subtle lesions and on epileptic patents to clarify some aspects of this condition that are still under debate.

REFERENCES

1. Cheng HL, Stikov N, Ghugre NR, Wright GA. Practical medical applications of quantitative MR relaxometry. J Magn Reson Imaging 2012; 36:805-24.
2. Robertson ID. Magnetic resonance imaging features of brain disease in small animals. In Thrall D. Veterinary Diagnostic Radiology, ed Saunders, Elsevier. St. Luis, 2013; p. 204.
3. Deoni SC. Quantitative relaxometry of the brain. Top Magn Reson Imaging 2010; 21:101-13.
4. Blystad I, Warntjes JBM, Smedby O, Lundberg P, Larsson EM, Tisell A. Quantitative MRI for analysis of peritumoral edema in malignant gliomas. Plos One 2017; 12(5):e0177135.
5. Chen H, Yu GL, Wang JT, Li F, Li GM. Application of T2 relaxometry in lateralization and localization of mesial temporal lobe epilepsy and corresponding comparison with MR volumetry. Acta Radiol 2016; 57:1107-13.
6. Sato S, Iwasaki M, Suzuki H, et al. T2 relaxometry improves detection of non-sclerotic epileptogenic hippocampus. Epilepsy Res 2016; 126:1-9.
7. Gillmann C, Coras R, Rossler K, Doerfler A, Uder M, Blumcke I, Bäuerle T. Ultra-high field MRI of human hippocampi: Morphological and multiparametric differentiation of hippocampal sclerosis subtypes. Plos One 2018; 13(4):e0196008.
8. Steenwijk MD, Vrenken H, Jonkman LE, Daams M, Geurts JJ, Barkhof F, Pouwels PJ. High-resolution T1-relaxation time mapping displays subtle, clinically relevant, gray matter damage in long-standing multiple sclerosis. Mult Scler J 2016; 22:1279-88.
9. Dean DC, Hurley SA, Kecskemeti SR, et al. Association of amyloid pathology with myelin alteration in preclinical alzheimer disease. Jama Neurol 2017; 74:41-49.
10. Pyatigorskaya N, Sharman M, Corvol JC, et al. High nigral iron deposition in LRRK2 and Parkin mutation carriers using R2*relaxometry. Mov Disord 2015; 30:1077-84.
11. Kamman RL, Go KG, Berendsen HJC. Nuclear magnetic resonance relaxation in experimental brain edema: effects of water concentration, protein concentration, and temperature. Magn Reson Med 1988; 6:265-74.
12. Hoehnberlage M, Tolxdorff T, Bockhorst K, Okada Y, Ernestus RI. In vivo nmr t(2) relaxation of experimental brain-tumors in the cat - a multiparameter tissue characterization. Magn Reson Imaging 1992; 10:935-47.
13. Samsonov A, Alexander AL, Mossahebi P, Wu CY, Duncan ID, Field AS. Quantitative MR imaging of two-pool magnetization transfer model parameters

in myelin mutant shaking pup. NeuroImage 2012; 1390-98.

14. Lorincz BA, Anson A, Csebi P, et al. Novel approach to magnetic resonance imaging of epileptic dogs-t2 relaxometry of the brain with emphasised hippocampus. Acta Vet Hung 2017; 65:185-97.
15. Konar M, Lang J. Pros and cons of low-field magnetic resonance imaging in veterinary practice. Vet Radiol Ultrasound 2011; 52(1 Suppl 1):S5-S14
16. Paus T, Collins DL, Evans AC, Leonard G, Pike B, Zijdenbos A. Maturation of white matter in the human brain: A review of magnetic resonance studies. Brain Res Bull 2001; 54:255-66.
17. Lagarias JC, Reeds JA, Wright MH, Wright PE. Convergence properties of the Nelder-Mead simplex method in low dimensions. SIAM J Optim 1998; 9:112-47.
18. Owen M. Radiographic, computed tomography and magnetic resonance imaging contrast media. In Thrall D. Veterinary Diagnostic Radiology, ed Saunders, Elsevier. St. Luis, 2013; p. 104.
19. Razek AAKA , Alvarez H, Bagg S, Refaat S, Castillo M. Imaging Spectrum of CNS Vasculitis. Radioraphics 2014; 34:873-94.
20. Swann JW, Priestnall SL, Dawson C, Chang YM, Garden OA. Histologic and clinical features of primary and secondary vasculitis: a retrospective study of 42 Dogs (2004-2011). J Vet Diagn Invest 2015; 27(4):489-96.
21. Crawford MA, Foil CS. Vasculitis: clinical syndromes in small animals. Compend Contin Educ Pract 1989; 11:400-415.
22. Snyder PW, Kazacos EA, Scott-Moncrieff JC, HogenEsch H, Carlton WW, Glickman LT, Felsburg PJ. Pathologic features of naturally occurring juvenile polyarteritis in beagle dogs. Vet Pathol 1995; 32:337-45.
23. Sasaki M, Pool R, Summers BA. Vasculitis in a dog resembling isolated angiitis of the central nervous system in humans. Vet Pathol 2003; 40:95-97.
24. Rusbridge C, Long S, Jovanovik J, et al. International Veterinary Epilepsy Task Force recommendations for a veterinary epilepsy-specific MRI protocol. BMC Vet Res 2015; 11:194.
25. Heiland S, Sartor K, Martin E, Bardenheuer HJ, Plaschke K. In vivo monitoring of age-related changes in rat brain using quantitative diffusion magnetic resonance imaging and magnetic resonance relaxometry. Neurosci Lett 2002; 334:157-60.
26. Guidotti R, Sinibaldi R, De Luca C, et al. Optimized 3D co-registration of ultra-low- field and hig field magnetic resonance images. Plos One 2018; 13(3):e019389020182018.
27. Sinibaldi R, Conti A, Sinjari B et al., Multimodal 3D imaging based on μMRI and μCT techiniques bridges the gap with histology in visualization of the bone regeneration process. J Tissue Eng Regen Med. 2018; 12(3):750-61.
28. Pownder SL, Hyashi K, Caserto BG, Breghner RE, Norman ML, Potter HG, Koff MF. Quantitative magnetic resonance imaging and histological comparison of normal canine menisci. Vet Comp Orthop Traumatol 2018; 31(6):452-57.